

Astability *versus* Bistability in van der Waals Tunnel Diode for Voltage Controlled Oscillator and Memory Applications

Nithin Abraham,[†] Krishna Murali,[†] Kenji Watanabe,[‡] Takashi Taniguchi,[¶] and
Kausik Majumdar^{*,†}

[†]*Department of Electrical Communication Engineering, Indian Institute of Science,
Bangalore 560012, India*

[‡]*Research Center for Functional Materials, National Institute for Materials Science, 1-1
Namiki, Tsukuba 305-0044, Japan*

[¶]*International Center for Materials Nanoarchitectonics, National Institute for Materials
Science, 1-1 Namiki, Tsukuba 305-0044, Japan*

E-mail: kausikm@iisc.ac.in

Abstract

Van der Waals (vdW) tunnel junctions are attractive due to their atomically sharp interface, gate tunability, and robustness against lattice mismatch between the successive layers. However, the negative differential resistance (NDR) demonstrated in this class of tunnel diodes often exhibits noisy behaviour with low peak current density, and lacks robustness and repeatability, limiting their practical circuit applications. Here we propose a strategy of using a 1L-WS₂ as an optimum tunnel barrier sandwiched in a broken gap tunnel junction of highly doped black phosphorus (BP) and SnSe₂. We achieve high yield tunnel diodes exhibiting highly repeatable, ultra-clean, and gate

tunable NDR characteristics with a signature of intrinsic oscillation, and a large peak-to-valley current ratio (PVCR) of 3.6 at 300 K (4.6 at 7 K), making them suitable for practical applications. We show that the thermodynamic stability of the vdW tunnel diode circuit can be tuned from astability to bistability by altering the constraint through choosing a voltage or a current bias, respectively. In the astable mode under voltage bias, we demonstrate a compact, voltage controlled oscillator without the need for an external tank circuit. In the bistable mode under current bias, we demonstrate a highly scalable, single element one-bit memory cell that is promising for dense random access memory applications in memory intensive computation architectures.

Keywords

tunnel diode, van der Waals heterostructure, negative differential resistance, voltage controlled oscillator, random access memory.

Nonlinear electronic devices play a pivotal role in wide ranging applications including oscillators, amplifiers, switching elements,^{1,2} and more recently in neural networks.^{3,4} Devices exhibiting negative differential resistance (NDR) characteristics, where a negative correlation exists between device current and voltage, are excellent candidates for these interesting applications. Following the landmark discovery by Esaki,⁵ tunnel diodes employing band-to-band tunneling (BTBT) have been an active area of research due to their NDR behaviour and ultra-fast response owing to the tunnelling nature of the carrier transport. Maintaining a sharp junction with a steep doping gradient is a key factor in achieving high tunneling efficiency in a tunnel diode. In this context, two-dimensional layered materials and their van der Waals (vdW) heterojunctions are highly promising⁶⁻¹⁷ due to their atomically sharp junctions, which can substantially reduce the process complexity and cost as opposed to bulk semiconductors. The wide collection of layered materials allows us to choose the desirable band offset in a vdW heterojunction without worrying about the lattice mismatch between two successive layers,^{18,19} providing a tremendous advantage over bulk semiconductors. In addition, tunnel diodes with the ultra-thin layers provide strong gate tunability⁶⁻¹⁵ - a trait which is usually unavailable in conventional tunnel diodes.

However, in a vdW heterojunction, the absence of a conventional depletion region due to ultra-thin nature of the layers, and atomic sharpness of the interface, prevents a voltage drop at the tunnel junction which degrades the NDR characteristics. This is because, for NDR to be observable, the tunneling current through the p - n junction must be tunable which requires a voltage modulation of the spectral overlap between the filled states at the conduction band of n -side and the empty states at the valence band of p -side. One thus requires the presence of a spatial gap between the n and p regions created during the transfer process or unintentional oxidation or a tunnel barrier that acts like an artificial depletion region to accommodate the required voltage drop at the tunnel junction. Relying on these processes takes a toll on the device yield, and the achieved NDR characteristics are inferior compared to state of the art Si and III-V semiconductor based tunnel diodes,^{20,21} in terms

of limited peak current density, poor repeatability, and large noise present in the tunneling current. This has led to limited efforts to use vdW heterojunction based tunnel diodes in real life applications,^{6,8} and thus non-Esaki vdW devices are being explored to achieve NDR.²²

In this work, by optimizing the tunnel barrier layer and using a clean device fabrication technique that maintains the high quality of the interfaces, we demonstrate a SnSe₂/1L-WS₂/BP vdW heterostructure based broken gap tunnel diode that exhibits ultra-clean, highly repeatable, and gate tunable NDR characteristics with a large peak-to-valley ratio (PVCR). We also show that the thermodynamic stability of the tunnel diode circuit in the NDR regime can be switched by changing the external constraint from voltage bias to a current bias. This allows us to further demonstrate a reactive element free persistent oscillation in an astable mode and a highly scalable memory cell in a bistable mode of operation of the vdW heterojunction tunnel diode.

Results and Discussions

Architecture of the SnSe₂/1L-WS₂/BP tunnel diode is schematically illustrated in Figure 1a. Mechanically exfoliated multi-layer SnSe₂ flakes are identified by optical contrast and are dry transferred on to pre-patterned Au electrodes. 1L-WS₂ and multi-layer BP flakes are stacked over the SnSe₂ flake with precise alignment following the same method. The other end of the BP layer is in contact with another Au electrode. The entire stack is immediately capped with a few-layer-thick hBN flake. The hBN flake serves the dual role of a protective capping for the BP flake^{23,24} and that of a gate dielectric. The top gate contact is defined using a few-layer graphene flake which is connected to a third Au electrode. The flakes are characterized using Raman spectroscopy as shown in **Supplementary Figure 1**. The fabrication approach we employ here utilising pre-patterned contacts does not require any chemical processing step after the flake transfer, and thus preserves the pristine nature of the BP interface. More details of the fabrication process are given in **Methods** and

illustrated stepwise in **Supplementary Figure 2**. A representative optical image of the stack is shown in Figure 1b. The Au electrode contacting the SnSe₂ (BP) flake is referred to as the source (drain) contact throughout the text. We measure the drain current (I_D) by applying an external voltage (V_D) at the drain contact, keeping the source terminal grounded. Seven such tunnel diodes (D1-D7) are fabricated, and all the devices exhibit repeatable NDR characteristics (summarized in **Supplementary Table 1**), pointing to the high yield of the fabrication process.

Band extrema of interest occur at the Z valley for BP²⁵ valance band and at the L valley for SnSe₂²⁶ conduction band as shown in Figure 1c. The presence of vacancies and impurities induce a large p -type doping in BP^{27,28} and a large n -type doping in SnSe₂.¹⁷ The degenerate doping and large band offsets between BP⁶ and SnSe₂^{7,29–31} result in a type-III (broken gap) band alignment at the heterojunction¹⁷ (Figure 1d). Under forward bias, the electrons experience inelastic band-to-band tunneling (BTBT) from the filled states of SnSe₂ conduction band to the empty states of BP valance band through the monolayer-thick WS₂ tunnel barrier. The current - voltage (I_D - V_D) characteristics of the tunnel junction D1 at 300 K is shown in Figure 1e, indicating a large current under reverse bias (Zener mode) and conspicuous NDR characteristics under forward bias (Esaki mode) - a direct evidence of BTBT dominated carrier transport.⁵ The band alignment in the heterojunction under different regions of operation is depicted in Figure 1f. Under forward bias, I_D increases linearly with V_D at low bias (region I) to a “peak current” I_P (point II, at $V_D = V_P$), which is attributed to an increasing overlap between filled states in SnSe₂ conduction band and empty states in BP valance band. With further increase in V_D , I_D drops abruptly, and followed by a gradual reduction (region III) and another abrupt drop and then a slow decrease to a minimum “valley current” I_V (region IV, at $V_D = V_V$). Such decrease in I_D with an increase in V_D in between the peak and the valley points indicates the presence of NDR in the DC characteristics. This decrease in I_D is due to a reduction in the overlapping states beyond $V_D = V_P$. Beyond the valley point, I_D again increases with further increase in V_D , due to

an enhancement in the thermionic current over the BP/SnSe₂ barrier. The diode achieves a high PVCR ($\frac{I_P}{I_V}$) of 3.6 at 300 K. The abrupt drops in the I_D characteristics has not been observed to date in vdW tunnel diodes,^{6–17} and indicate the presence of oscillations in the diode³² which will be explained later.

As explained earlier, BP and SnSe₂ form a broken gap vdW heterojunction, which is ideally suited for high BTBT current. However in the absence of the 1L-WS₂ tunnel barrier, due to the high conductivity of such junction along with its atomic sharpness, there is a very little voltage drop across the junction. This forces the quasi-Fermi levels of the BP and the SnSe₂ sides to be almost aligned at the tunneling interface in spite of a change in the applied external bias. This degrades the PVCR, with a possibility of complete suppression of NDR characteristics, although the total tunneling current remains high. When we introduce the WS₂ sandwich layer, it acts like an atomically sharp depletion layer allowing a larger voltage to drop across it. This effectively de-pins the BP and SnSe₂ bands at the tunneling interface, allowing their relative movement which is crucial in observing the NDR characteristics.^{17,20} Clearly, it is critical to optimize the thickness of the barrier layer to achieve the optimum device performance. The results of tunnel diodes fabricated with different barrier layers [no barrier layer (D8), 1L-WS₂ (D1), 2L-WS₂ (D9), and 1L-MoS₂ (D10)] are summarized in **Supplementary Table 2**. We observe that the device with no barrier exhibits an order of magnitude higher tunneling current, however, with no NDR signature (**Supplementary Figure 3a**). The device with 2L-WS₂ as a barrier layer (**Supplementary Figure 3c**) exhibits a PVCR of ~ 2 , but with significantly suppressed tunneling current due to increased barrier width. An annealing step in the fabrication also helps in reducing the inter-layer spacing. As can be seen from samples D2 and D3 (**Supplementary Table 1**), the current density increases drastically with an annealing step after WS₂ transfer with no degradation of PVCR. The tunnelling current for 1L-MoS₂ (**Supplementary Figure 3d**) and 1L-WS₂ barrier devices are comparable, however, the NDR characteristics are far superior and cleaner in the latter case, likely due to higher defect density in MoS₂.^{33,34}

To investigate the current transport mechanisms at different regions of operation, we measure the I_D - V_D characteristics of the device D1 at various temperatures ranging from 7 K to 300 K, as shown in Figure 2a. A magnified view of the NDR region in linear scale is given in Figure 2b. The NDR characteristics and the low noise nature is maintained in the entire temperature range pointing to the stability of the processes and the high quality of the interfaces. The strong temperature dependence of the peak current points to a phonon-assisted inelastic tunneling process.^{35,36} This is in agreement with the fact that conduction band minimum at SnSe₂ being at the L point, while the valence band maximum of BP is at the Z point (see Figure 1d), requiring the assistance of phonon for in-plane momentum conservation during the tunnelling process.³⁷

Extracted temperature dependence of the peak and the valley currents and the corresponding voltages are given respectively in Figure 2c and d. Figure 2c shows that with a reduction in temperature, I_V reduces at a slightly faster rate than I_P , improving the PVCR to ~ 4.6 at low temperature. However, I_V appears to be a much weaker function of temperature than thermionic process, suggesting a non-thermionic origin of the valley current. To establish the point quantitatively, using Richardson equation,³⁸ we plot $\ln(\frac{I_V}{T^2})$ as a function of $\frac{1}{T}$ in Figure 2e. The positive slope observed clearly suggests that the valley current is not dominated by the thermionic current over the BP conduction band barrier. Such non-thermionic current at the valley is common in tunnel diode literature,^{39,40} and is usually attributed to the excess current. The excess current originates from carrier transport through the sub-bandgap states created by structural disorders and impurities, and several possible transport mechanisms are schematically illustrated in inset of Figure 2e. The carriers from either of the degenerate regions of BP or SnSe₂ can lose energy and drop to states in the otherwise forbidden band gap (paths A and B). These carriers then tunnel to the other side resulting in a nonzero valley current. The nonzero defect density present in the WS₂ barrier layer also acts as an intermediate state for the excess current (path C). Considering the bandgap (E_G) of 1L-WS₂ as the effective energy gap the carriers need to overcome to

generate the excess current, we first map the bandgap of 1L-WS₂ at different measurement temperatures,⁴¹ and then plot $\ln(I_V)$ as a function of the corresponding E_G in Figure 2f. The linear trend with negative slope provides further evidence of the defect induced excess current as the primary source of valley current.³⁹ The non-thermionic origin of I_V sets a lower bound on the valley current and hence causes the PVCR to saturate at low temperature, as shown in right axis of Figure 2c. The suppression of the excess current by reducing the defect density through the usage of higher quality flakes is thus of paramount importance to further reduce I_V and achieve a PVCR limit determined by the thermionic current.

In the presence of nonzero series resistance, the external bias required to achieve peak or valley configurations is given by

$$V_{P,V}(T) = V_{P,V}^0 + I_{P,V}(T) \times R_s(T) \quad (1)$$

where $V_{P,V}^0$ is the drop at the junction at peak or valley, and $R_s(T)$ is the temperature dependent series resistance. The measured V_P and V_V are shown in Figure 2d as a function of the temperature. The increase in V_P and V_V with a decrease in temperature results from an increase in R_s due to a lower injection efficiency at the contact.

We next measure the characteristics of the tunnel diode by varying V_G at a fixed temperature. V_G modulates the device response through two different ways: 1) it changes the extent of the p -doping of the BP layer at the junction and hence modulates the tunneling rate, 2) it tunes the lateral resistance R_s of the BP channel. For a thin BP layer, both these effects are significant. The response of one such device (sample D4, less than 10 nm thick BP) at 300 K is shown in Figure 3a. Modulation of I_P and I_V with V_G is given in the left axis of Figure 3b. I_P increases with more negative V_G due to an enhancement in the p -doping of the BP layer, as illustrated using the band diagram I in Figure 3c. An increased p -doping at the tunneling interface results in a larger overlap between the filled states in the conduction band of SnSe₂ and the empty states of BP valance band and thus a larger I_P .

Similarly, an increasingly positive V_G results in a reduced p -doping in BP as shown in Figure 3c (II and III), and hence lowers I_P . I_V being dominated by the excess current remains largely independent of V_G as expected. The modulation of the doping also affects the lateral resistance R_s of the device and causes the peak and valley to occur at a larger voltage with an increase in positive V_G (right axis of Figure 3b). A similar observation is made for the device response at 4.7 K given in **Supplementary Figure 4**.

To decouple the effects of tunneling rate and series resistance, we measure the response from a device employing a thick (~ 20 nm) BP layer (sample D1) at 7 K, and the results are summarized in Figure 3d-f. I_P and I_V and hence the PVCR remain independent of V_G , as shown in left axis of Figure 3e. I_P being limited by the overlap of the available states for tunneling, its invariance with V_G suggests that the local hole density near the tunneling interface in the BP layer remains independent of V_G due to screening.⁴² The shift of V_P and V_V with varying V_G (right axis of Figure 3e) without any change in I_P and I_V indicates a change in the series resistance with V_G . As V_G becomes more negative, the BP channel becomes more p -doped (region I). This reduces R_s and hence the external bias required to align the junction for peak current drops, as seen in Figure 3e. On the other hand, a small positive V_G (region II) reduces the p -type doping in the BP channel and hence increases the lateral resistance leading to an increase in V_P . This trend follows till $V_D \approx 1.5$ V. For larger positive V_G (region III), the trend turns around and V_P starts decreasing. Due to the ambipolar nature of BP, at large positive V_G , the top gate interface of the BP channel turns electron rich, while a hole rich channel near the bottom tunneling interface is retained. This leads to the formation of an electron-hole (e-h) bilayer along the vertical direction,⁴³ as schematically shown in Figure 3f. In the e-h bilayer, both the layers act as parallel channels of transport, but employing different types of carriers. The carrier can switch its nature by tunnelling across the barriers formed between n^+ and p^+ regions of BP. This process occurs efficiently due to the small and direct nature of BP bandgap.⁴⁴ This effect reduces the lateral resistance at higher positive V_G and reduces V_P . Due to the smaller magnitude of I_V , the

relative change in the potential drop across the series resistance is less at the valley position, resulting in a weaker gate modulation of V_V .

The different rates of modulation for peak and valley positions lead to a gate dependent NDR window, importance of which will be explained later in a memory device. This also tunes the slope of the current in the NDR region and hence results in a gate controllable ac resistance. Such a modulation of the ac resistance is imperative in NDR based amplifier circuits⁴⁵ where the gain of the amplifier can be controlled by a gate bias.

NDR devices find widespread application in oscillator circuits, where the negative differential resistance of the device is used to compensate the stray resistance in the tank circuit, resulting in an undamped oscillation.^{46,47} However, the dependency on an external tank circuit to create oscillation is the limiting factor for large output power at high frequency.^{48–50} In the quest for intrinsic oscillator without external reactive elements, the astable nature of the NDR region is explored by measuring the output characteristics with different measurement speeds. The results of a slow (10 samples/sec) I_D measurement as a function of the bias V_D for D1 is given in the top panel of Figure 4a as the blue trace. On reducing the integration time for each sample point (200 samples/sec), we observe an I_D oscillating between I_P and I_V as shown by the green trace in Figure 4a. During the slow measurement, the obtained current is a time-average of the fluctuating current. Outside this unstable region, the current measured with both configurations overlap each other perfectly.

The measured average power delivered to the entire system (illustrated in bottom panel of Figure 4a) also shows *N-shape* characteristics, pointing to the thermodynamic instability in the NDR regime. This results in the multi-valued nature of the voltage output for a given power delivered. The interplay between the positive feedback in the unstable regime and the restoring force by the fixed external voltage bias leads to the observed oscillation. Note that the absence such thermodynamic instability in a device with 2L-WS₂ as the barrier rules out the possibility of sustained oscillation even though it exhibits a comparable PVCR (see **Supplementary Figure 5**).

We now bias the tunnel diode at a fixed V_D in the NDR region, and measure the oscillating voltage across the diode using a digital storage oscilloscope as shown in Figure 4b.³² The nonzero cabling and setup resistance R_w from the tunnel diode to the SMU allows the voltage across the diode to fluctuate and show up across the oscilloscope probe. The measured temporal response at three different V_D values is shown in Figure 4c, indicating stable and persistent oscillation. Such an astable operation helps in realizing single element oscillator where the need for integrating reactive elements on chip can be avoided. Proximity of the biasing point to either of peak or valley modulates the duration for which the circuit latches near that particular state, modulating the duty cycle and frequency of oscillation, as shown in Figure 4d. This can be seen as slower initial rise for a bias of $V_D = 0.110$ V and a slow initial fall for $V_D = 0.255$ V (bottom and top panels in Figure 4c). The system reaches a maximum frequency when biased in the middle of the NDR region as the restoring forces are maximum. The tuning of the oscillation frequency by the applied bias is shown in **Supplementary Video 1**. Note that, the large stray capacitance of the cable and the probe station (~ 75 pF) limits the observed frequency of oscillation, while the intrinsic frequency is much higher. A reduction in the stray capacitance in the circuit coupled with an enhancement in the peak current density would help to attain a higher frequency. These oscillations are stable over long duration as observed from different measurements (different panels in **Supplementary Figure 6**) and survive at low temperature as well, as shown in **Supplementary Figure 7**.

We now investigate the possibility of obtaining a bistable operation from the tunnel diode for random access memory (RAM) applications. This is achieved by forcing I_D across the tunnel diode terminals and measuring the voltage drop across it, as shown in the left axis of Figure 5a (in blue trace). The forward and reverse sweeps are indicated by the black arrows. The result from a voltage sweep is also shown as dashed orange trace for reference. When the forcing current is increased beyond I_P , the voltage across the diode jumps to the positive differential resistance branch beyond the valley point. After this jump, when the

current bias is reduced, the voltage does not trace back in the same path, rather remains in the positive resistance branch until a current bias value of I_V . When current bias is reduced below I_V , the voltage abruptly drops to the other positive differential resistance branch below the peak point. Hence the output voltage is multi-valued for a given range of current bias, and its value depends on the history of the device. This gives the device the ability to store information equivalent of one bit encoded in the voltage across it. The stored value of the junction can be altered by forcing positive or negative current spikes that ride on the biasing current. To retrieve the stored bit value, just monitoring the voltage across the device is sufficient, cutting down the extra elements required in conventional memories. A voltage value above V_V and below V_P corresponds to a stored value of logic ‘1’ and logic ‘0’ respectively (Figure 5a).

The thermodynamic origin of the bistable states can be understood from extracting the power delivered to the circuit at each current bias, as shown by the red circles in the right axis of Figure 5a. In between I_P and I_V , at a given current bias, there are two metastable states of the system separated by an energy barrier. This is in stark contrast with the previously discussed astable oscillation at a given voltage bias. It is striking that by changing the constraint (voltage or current bias), the thermodynamic stability of the system can be effectively tuned between astability to bistability.

The logic state stored in the memory cell should be less susceptible to external noise sources and the read operation should be able to distinguish the state of the system with confidence. Thus, the threshold for switching between logics ‘0’ and ‘1’ is an important metric. The separation $I_P - I_V$ corresponds to the maximum allowed peak to peak fluctuation, and determines the stored bit retention. For device D4 with thin BP, I_P being strongly dependent on V_G , results in a gate tunable $I_P - I_V$ as shown in Figure 5b. A negative gate bias is able to enhance the range by $\sim 180\%$ making the memory cell more immune to external noise. On the other hand, the separation $V_V - V_P$ indicates the stability against noise during the read operation. Our ability to modulate the series resistance using V_G allows

this separation to be effectively tuned, as shown in Figure 5c-d for device D5 with a thick BP channel. The tunable noise margins thus obtained has a trade off with the operating frequency as well as both the standby and dynamic power consumption. This can be used in designing an intelligent memory architecture that dynamically decides the noise margin providing optimum speed and power consumption.

The proposed memory cell with a junction area of 400 nm^2 is expected to exhibit a standby power of 0.33 pW (3.13 pW) when retaining logic ‘0’ (logic ‘1’), which is significantly less compared with the state of the art Intel 22 nm HDC Tri-gate LP SRAM cell ($\sim 40\text{ pW}$).⁵¹ On the other hand, the single element and vertical design of the heterojunction memory allows us to reduce the footprint per cell dramatically, providing about 100 times higher packing density. The additional possibility of stacking multiple heterojunctions vertically using 3D integration brings about a great density advantage compared to the state of the art SRAM. This is promising for next generation architectures like memory intensive computing and bio-inspired computing.

Conclusion

In conclusion, we report a broken gap van der Waals heterojunction based tunnel diode exhibiting clean, repeatable, and gate tunable negative differential resistance characteristics with a high peak-to-valley ratio over a large temperature range. By altering the constraint from constant voltage to constant current bias, the thermodynamic stability of the tunnel diode circuit is tuned from astability to bistability. This allows us to demonstrate multifunctional operations like a reactive-element-less on chip, compact voltage controlled oscillator, and a highly scalable, single element random access memory cell for ultra-dense memory applications. The operations are sustained at very low temperature, making them attractive for cryogenic electronics as well.

Methods

Fabrication

Au lines are defined by optical lithography using a 360 nm UV source and AZ5214E resist spin-coated on an Si/SiO₂ substrate with 285 nm thick oxide formed by dry chlorinated thermal oxidation and forming gas annealing. A 20 nm thick Ni film followed by a 40 nm thick Au film is deposited *via* DC magnetron sputtering and lifted off by Acetone/iso-propyl alcohol rinse to form the bottom contact. The SnSe₂ flakes are exfoliated from bulk crystals using Scotch tape, and are subsequently transferred to a poly-di-methyl-siloxane (PDMS) sheet. Flakes of thickness ~ 50 nm are identified by optical contrast and transferred onto the Au line forming source contact using a dry transfer technique. This process is performed underneath a microscope using controlled translation and rotation for desired positioning of the flakes with respect to the pre-patterned substrate. This process is repeated for monolayer WS₂. The SnSe₂/WS₂ stack is annealed at 70°C for 2 min in ambient for devices D1, D2, D4 and D6. BP of thickness ~ 20 nm is transferred next contacting another Au line forming drain contact. The stack is immediately encapsulated with hBN following the BP transfer. For devices D3 and D5, the stack is annealed after hBN transfer. Few layer graphene is transferred to form the gate contact. The layers in the whole device fabrication process do not undergo any chemical treatment and hence maintain their pristine quality and clean interfaces.

Characterization

The devices are loaded into a closed cycle He probe station Lakeshore CRX-6.5K or are wire bonded to a closed cycle He cryostat and characterized using a Keithley 4200A SCS parameter analyser for DC measurements and a Tektronix MDO3000 digital storage oscilloscope for frequency measurements. All the measurements were done in vacuum with a pressure $< 10^{-4}$ Torr.

Acknowledgements

K. M. acknowledges the support a grant from Indian Space Research Organization (ISRO), a grant from MHRD under STARS, grants under Ramanujan Fellowship and Nano Mission from the Department of Science and Technology (DST), Government of India, and support from MHRD, MeitY and DST Nano Mission through NNetRA. K.W. and T.T. acknowledge support from the Elemental Strategy Initiative conducted by the MEXT, Japan, Grant Number JPMXP0112101001, JSPS KAKENHI Grant Numbers JP20H00354 and the CREST(JPMJCR15F3), JST.

Supporting Information

The Supporting Information is available on: Raman characterization of flakes; Fabrication steps; Summary of results from multiple devices and different barrier layers; Gate dependence of output characteristics of sample D4 at 4.7 K; Absence of oscillation for heterostructure with thick barrier layer; Persistence and stability of oscillations; Astable operation at 7 K; Video showing modulation of oscillation frequency as a function of bias voltage.

Competing Interest

The authors declare no financial or non-financial competing interest.

References

1. Feiginov, M.; Sydlo, C.; Cojocari, O.; Meissner, P. Resonant-Tunnelling-Diode Oscillators Operating at Frequencies above 1.1 THz. *Appl. Phys. Lett.* **2011**, *99*, 233506.
2. Peng, H. Y.; Li, Y. F.; Lin, W. N.; Wang, Y. Z.; Gao, X. Y.; Wu, T. Deterministic

- Conversion between Memory and Threshold Resistive Switching *via* Tuning the Strong Electron Correlation. *Sci. Rep.* **2012**, *2*, 442.
3. Tanaka, H.; Akai-Kasaya, M.; TermehYousefi, A.; Hong, L.; Fu, L.; Tamukoh, H.; Tanaka, D.; Asai, T.; Ogawa, T. A Molecular Neuromorphic Network Device Consisting of Single-Walled Carbon Nanotubes Complexed with Polyoxometalate. *Nat. Commun.* **2018**, *9*, 2693.
 4. Pickett, M. D.; Medeiros-Ribeiro, G.; Williams, R. S. A Scalable Neuristor Built with Mott Memristors. *Nat. Mater.* **2013**, *12*, 114–117.
 5. Esaki, L. New Phenomenon in Narrow Germanium $p - n$ Junctions. *Phys. Rev.* **1958**, *109*, 603–604.
 6. Shim, J.; Oh, S.; Kang, D.-H.; Jo, S.-H.; Ali, M. H.; Choi, W.-Y.; Heo, K.; Jeon, J.; Lee, S.; Kim, M.; Song, Y. J.; Park, J.-H. Phosphorene/Rhenium Disulfide Heterojunction-Based Negative Differential Resistance Device for Multi-Valued Logic. *Nat. Commun.* **2016**, *7*, 13413.
 7. Fan, S.; Vu, Q. A.; Lee, S.; Phan, T. L.; Han, G.; Kim, Y.-M.; Yu, W. J.; Lee, Y. H. Tunable Negative Differential Resistance in van der Waals Heterostructures at Room Temperature by Tailoring the Interface. *ACS Nano* **2019**, *13*, 8193–8201.
 8. Nourbakhsh, A.; Zubair, A.; Dresselhaus, M. S.; Palacios, T. Transport Properties of a $\text{MoS}_2/\text{WSe}_2$ Heterojunction Transistor and Its Potential for Application. *Nano Lett.* **2016**, *16*, 1359–1366.
 9. Movva, H. C. P.; Kang, S.; Rai, A.; Kim, K.; Fallahazad, B.; Taniguchi, T.; Watanabe, K.; Tutuc, E.; Banerjee, S. K. Room Temperature Gate-Tunable Negative Differential Resistance in $\text{MoS}_2/\text{hBN}/\text{WSe}_2$ Heterostructures. *2016 74th Annu. Device Res. Conf.* **2016**, 1–2.

10. Duong, N. T.; Bang, S.; Lee, S. M.; Dang, D. X.; Kuem, D. H.; Lee, J.; Jeong, M. S.; Lim, S. C. Parameter Control for Enhanced Peak-to-Valley Current Ratio in a MoS₂/MoTe₂ van der Waals Heterostructure. *Nanoscale* **2018**, *10*, 12322–12329.
11. Jia, J.; Xu, J.; Park, J.-H.; Lee, B. H.; Hwang, E.; Lee, S. Multifunctional Homogeneous Lateral Black Phosphorus Junction Devices. *Chem. Mater.* **2017**, *29*, 3143–3151.
12. Srivastava, P. K.; Hassan, Y.; Gebredingle, Y.; Jung, J.; Kang, B.; Yoo, W. J.; Singh, B.; Lee, C. Multifunctional van der Waals Broken-Gap Heterojunction. *Small* **2019**, *15*, 1804885.
13. Fan, S.; Yun, S. J.; Yu, W. J.; Lee, Y. H. Tailoring Quantum Tunneling in a Vanadium-Doped WSe₂/SnSe₂ Heterostructure. *Adv. Sci.* **2020**, *7*, 1902751.
14. Roy, T.; Tosun, M.; Cao, X.; Fang, H.; Lien, D.-H.; Zhao, P.; Chen, Y.-Z.; Chueh, Y.-L.; Guo, J.; Javey, A. Dual-Gated MoS₂/WSe₂ van der Waals Tunnel Diodes and Transistors. *ACS Nano* **2015**, *9*, 2071–2079.
15. Lee, J.; Duong, N. T.; Bang, S.; Park, C.; Nguyen, D. A.; Jeon, H.; Jang, J.; Oh, H. M.; Jeong, M. S. Modulation of Junction Modes in SnSe₂/MoTe₂ Broken-Gap van der Waals Heterostructure for Multifunctional Devices. *Nano Lett.* **2020**, *20*, 2370–2377.
16. Roy, T.; Tosun, M.; Hettick, M.; Ahn, G. H.; Hu, C.; Javey, A. 2D-2D Tunneling Field-Effect Transistors Using WSe₂/SnSe₂ Heterostructures. *Appl. Phys. Lett.* **2016**, *108*, 83111.
17. Yan, R.; Fathipour, S.; Han, Y.; Song, B.; Xiao, S.; Li, M.; Ma, N.; Protasenko, V.; Muller, D. A.; Jena, D.; Xing, H. G. Esaki Diodes in van der Waals Heterojunctions with Broken-Gap Energy Band Alignment. *Nano Lett.* **2015**, *15*, 5791–5798.
18. Geim, A. K.; Grigorieva, I. V. van der Waals Heterostructures. *Nature* **2013**, *499*, 419–425.

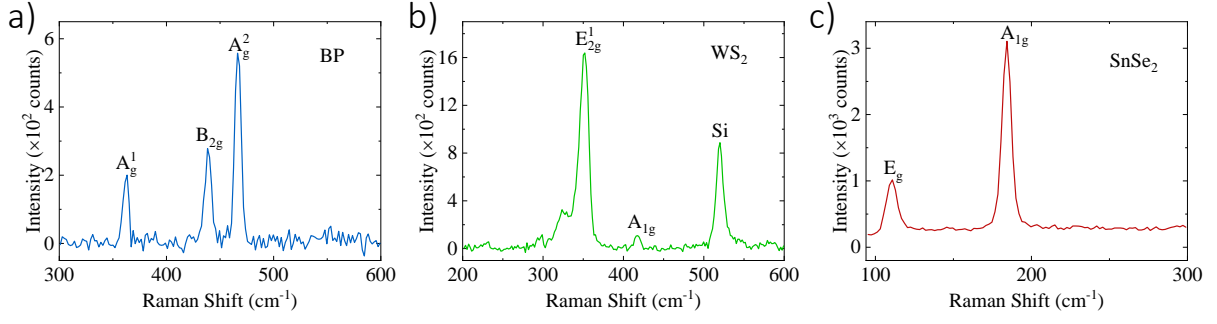
19. Liu, Y.; Weiss, N. O.; Duan, X.; Cheng, H.-C.; Huang, Y.; Duan, X. van der Waals Heterostructures and Devices. *Nat. Rev. Mater.* **2016**, *1*, 16042.
20. Pawlik, D.; Romanczyk, B.; Thomas, P.; Rommel, S.; Edirisooriya, M.; Contreras-Guerrero, R.; Droopad, R.; Loh, W.; Wong, M. H.; Majumdar, K.; Wang, W. .; Kirsch, P. D.; Jammy, R. Benchmarking and Improving III-V Esaki Diode Performance with a Record 2.2 MA/cm² Peak Current Density to Enhance TFET Drive Current. *IEEE Int. Electron Devices Meet., 2012* **2012**, 27.1.1–27.1.3.
21. Oehme, M.; Hähnel, D.; Werner, J.; Kaschel, M.; Kirfel, O.; Kasper, E.; Schulze, J. Si Esaki Diodes with High Peak to Valley Current Ratios. *Appl. Phys. Lett.* **2009**, *95*, 242109.
22. Mahajan, M.; Majumdar, K. Gate- and Light-Tunable Negative Differential Resistance with High Peak Current Density in 1T-TaS₂/2H-MoS₂ T-Junction. *ACS Nano* **2020**, *14*, 6803–6811, PMID: 32406676.
23. Doganov, R. A.; O’Farrell, E. C. T.; Koenig, S. P.; Yeo, Y.; Ziletti, A.; Carvalho, A.; Campbell, D. K.; Coker, D. F.; Watanabe, K.; Taniguchi, T.; Neto, A. H. C.; Özyilmaz, B. Transport Properties of Pristine Few-Layer Black Phosphorus by van der Waals Passivation in an Inert Atmosphere. *Nat. Commun.* **2015**, *6*, 6647.
24. Avsar, A.; Vera-Marun, I. J.; Tan, J. Y.; Watanabe, K.; Taniguchi, T.; Castro Neto, A. H.; Özyilmaz, B. Air-Stable Transport in Graphene-Contacted, Fully Encapsulated Ultrathin Black Phosphorus-Based Field-Effect Transistors. *ACS Nano* **2015**, *9*, 4138–4145.
25. Qiao, J.; Kong, X.; Hu, Z.-X.; Yang, F.; Ji, W. High-Mobility Transport Anisotropy and Linear Dichroism in Few-Layer Black Phosphorus. *Nat. Commun.* **2014**, *5*, 4475.
26. Gonzalez, J. M.; Oleynik, I. I. Layer-Dependent Properties of SnS₂ and SnSe₂ Two-Dimensional Materials. *Phys. Rev. B* **2016**, *94*, 125443.

27. Kiraly, B.; Hauptmann, N.; Rudenko, A. N.; Katsnelson, M. I.; Khajetoorians, A. A. Probing Single Vacancies in Black Phosphorus at the Atomic Level. *Nano Lett.* **2017**, *17*, 3607–3612.
28. Gaberle, J.; Shluger, A. L. Structure and Properties of Intrinsic and Extrinsic Defects in Black Phosphorus. *Nanoscale* **2018**, *10*, 19536–19546.
29. Aretouli, K. E.; Tsoutsou, D.; Tsipas, P.; Marquez-Velasco, J.; Aminalragia Giamini, S.; Kelaidis, N.; Psycharis, V.; Dimoulas, A. Epitaxial 2D SnSe₂/ 2D WSe₂ van der Waals Heterostructures. *ACS Appl. Mater. Interfaces* **2016**, *8*, 23222–23229.
30. Krishna, M.; Kallatt, S.; Majumdar, K. Substrate Effects in High Gain, Low Operating Voltage SnSe₂ Photoconductor. *Nanotechnology* **2017**, *29*, 035205.
31. Murali, K.; Dandu, M.; Das, S.; Majumdar, K. Gate-Tunable WSe₂/SnSe₂ Backward Diode with Ultrahigh-Reverse Rectification Ratio. *ACS Appl. Mater. Interfaces* **2018**, *10*, 5657–5664, PMID: 29355302.
32. Jinli Wang,; Wheeler, D.; Yan, Y.; Jialin Zhao,; Howard, S.; Seabaugh, A. Silicon Tunnel Diodes Formed by Proximity Rapid Thermal Diffusion. *IEEE Electron Device Lett.* **2003**, *24*, 93–95.
33. Addou, R.; Colombo, L.; Wallace, R. M. Surface Defects on Natural MoS₂. *ACS Appl. Mater. Interfaces* **2015**, *7*, 11921–11929.
34. Bampoulis, P.; van Bremen, R.; Yao, Q.; Poelsema, B.; Zandvliet, H. J. W.; Sotthewes, K. Defect Dominated Charge Transport and Fermi Level Pinning in MoS₂/Metal Contacts. *ACS Appl. Mater. Interfaces* **2017**, *9*, 19278–19286.
35. Logan, R. A.; Chynoweth, A. G. Effect of Degenerate Semiconductor Band Structure on Current-Voltage Characteristics of Silicon Tunnel Diodes. *Phys. Rev.* **1963**, *131*, 89–95.

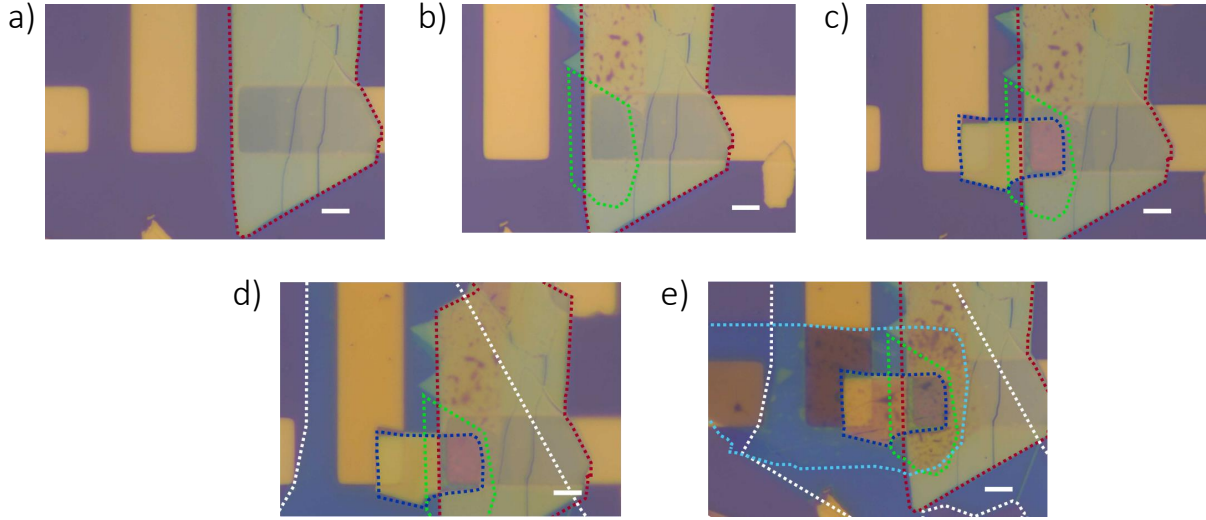
36. Dashiell, M. W.; Troeger, R. T.; Rommel, S. L.; Adam, T. N.; Berger, P. R.; Guedj, C.; Kolodzey, J.; Seabaugh, A. C.; Lake, R. Current-Voltage Characteristics of High Current Density Silicon Esaki Diodes Grown by Molecular Beam Epitaxy and the Influence of Thermal Annealing. *IEEE Trans. Electron Devices* **2000**, *47*, 1707–1714.
37. Kane, E. O. Theory of Tunneling. *J. Appl. Phys.* **1961**, *32*, 83–91.
38. Crowell, C. R. The Richardson Constant for Thermionic Emission in Schottky Barrier Diodes. *Solid. State. Electron.* **1965**, *8*, 395–399.
39. Chynoweth, A. G.; Feldmann, W. L.; Logan, R. A. Excess Tunnel Current in Silicon Esaki Junctions. *Phys. Rev.* **1961**, *121*, 684–694.
40. Majumdar, K.; Thomas, P.; Loh, W.; Hung, P.; Matthews, K.; Pawlik, D.; Romanczyk, B.; Filmer, M.; Gaur, A.; Droopad, R.; Rommel, S. L.; Hobbs, C.; Kirsch, P. D. Mapping Defect Density in MBE Grown $\text{In}_{0.53}\text{Ga}_{0.47}\text{As}$ Epitaxial Layers on Si Substrate Using Esaki Diode Valley Characteristics. *IEEE Trans. Electron Devices* **2014**, *61*, 2049–2055.
41. Nagler, P.; Ballottin, M. V.; Mitiglu, A. A.; Durnev, M. V.; Taniguchi, T.; Watanabe, K.; Chernikov, A.; Schüller, C.; Glazov, M. M.; Christianen, P. C. M.; Korn, T. Zeeman Splitting and Inverted Polarization of Biexciton Emission in Monolayer WS_2 . *Phys. Rev. Lett.* **2018**, *121*, 57402.
42. Li, L.; Yu, Y.; Ye, G. J.; Ge, Q.; Ou, X.; Wu, H.; Feng, D.; Chen, X. H.; Zhang, Y. Black Phosphorus Field-Effect Transistors. *Nat. Nanotechnol.* **2014**, *9*, 372–377.
43. Wu, P.; Appenzeller, J. Reconfigurable Black Phosphorus Vertical Tunneling Field-Effect Transistor with Record High ON-Currents. *IEEE Electron Device Lett.* **2019**, *40*, 981–984.

44. Xiong, X.; Huang, M.; Hu, B.; Li, X.; Liu, F.; Li, S.; Tian, M.; Li, T.; Song, J.; Wu, Y. A Transverse Tunnelling Field-Effect Transistor Made from a van der Waals Heterostructure. *Nat. Electron.* **2020**, *3*, 106–112.
45. Wang, M.; Wang, C.-Y.; Wu, C.; Li, Q.; Pan, C.; Wang, C.; Liang, S.-J.; Miao, F. S-Type Negative Differential Resistance in Semiconducting Transition-Metal Dichalcogenides. *Adv. Electron. Mater.* **2019**, *5*, 1800853.
46. Mishchenko, A.; Tu, J. S.; Cao, Y.; Gorbachev, R. V.; Wallbank, J. R.; Greenaway, M. T.; Morozov, V. E.; Morozov, S. V.; Zhu, M. J.; Wong, S. L.; Withers, F.; Woods, C. R.; Kim, Y.-J.; Watanabe, K.; Taniguchi, T.; Vdovin, E. E.; Makarovskiy, O.; Fromhold, T. M.; Fal’ko, V. I.; Geim, A. K. *et al.* Twist-Controlled Resonant Tunnelling in Graphene/Boron Nitride/Graphene Heterostructures. *Nat. Nanotechnol.* **2014**, *9*, 808–813.
47. Van Degrift, C. T.; Love, D. P. Modeling of Tunnel Diode Oscillators. *Rev. Sci. Instrum.* **1981**, *52*, 712–723.
48. Jonasson, O.; Knezevic, I. Coulomb-Driven Terahertz-Frequency Intrinsic Current Oscillations in a Double-Barrier Tunneling Structure. *Phys. Rev. B* **2014**, *90*, 165415.
49. Woolard, D. L.; Buot, F. A.; Rhodes, D. L.; Lu, X. J.; Lux, R. A.; Perlman, B. S. On the Different Physical Roles of Hysteresis and Intrinsic Oscillations in Resonant Tunneling Structures. *J. Appl. Phys.* **1996**, *79*, 1515–1525.
50. Zhao, P.; Woolard, D. L.; Cui, H. L.; Horing, N. J. M. Origin of Intrinsic Oscillations in Double-Barrier Quantum-Well Systems. *Phys. Lett. A* **2003**, *311*, 432–437.
51. Jan, C. H.; Bhattacharya, U.; Brain, R.; Choi, S. J.; Curello, G.; Gupta, G.; Hafez, W.; Jang, M.; Kang, M.; Komeyli, K.; Leo, T.; Nidhi, N.; Pan, L.; Park, J.; Phoa, K.; Rahman, A.; Staus, C.; Tashiro, H.; Tsai, C.; Vandervoorn, P. *et al.* A 22 nm SoC

Platform Technology Featuring 3-D Tri-Gate and High-K/Metal Gate, Optimized for Ultra Low Power, High Performance and High Density SoC Applications. *IEEE Int. Electron Devices Meet., 2012* **2012**, 3.1.1–3.1.4.



Supplementary Figure 1: **Raman characterization for different flakes:** Raman spectra of a) BP, b) WS_2 , c) $SnSe_2$, collected with 532 nm excitation.



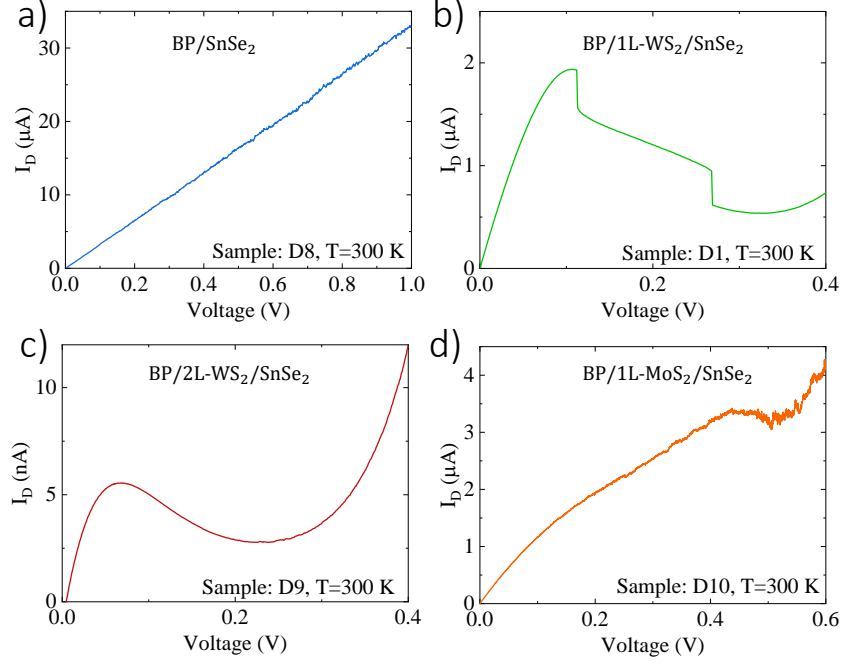
Supplementary Figure 2: **Fabrication steps for tunnel diode:** a) Transfer of $SnSe_2$ (Red dotted trace). b) Transfer of 1L- WS_2 with precise alignment (Green dotted trace). c) Transfer of few layer BP (Blue dotted trace). d) Encapsulation with hBN (White dotted trace). e) Transfer of graphene for gate contact (Cyan dotted trace). Scale bar is 5 μm .

Supplementary Table 1: Summary of tunnel diode performance from multiple samples using BP/1L-WS₂/SnSe₂ heterojunction

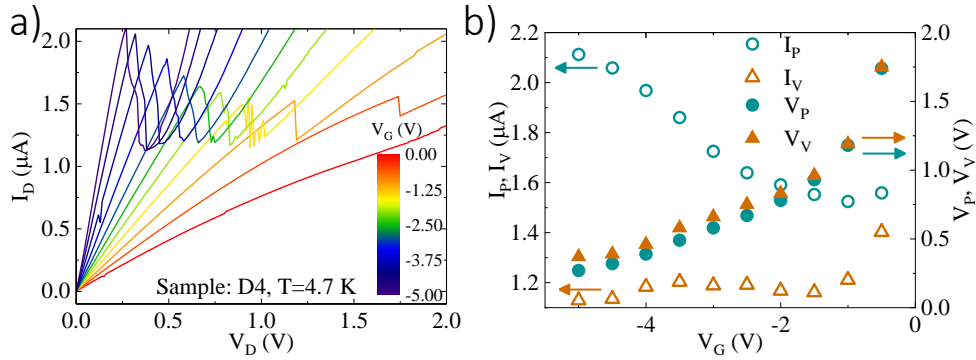
Device	Barrier	J_p (A/cm^2)	J_v (A/cm^2)	PVCR	Temperature (K)	Annealing
D1	1L WS ₂	2.68	0.74	3.60	300	After WS ₂
		1.74	0.38	4.58	7	
D2	1L WS ₂	18.07	5.56	3.25	300	After WS ₂
D3	1L WS ₂	0.08	0.03	3.00	300	Not annealed
		14.66	6.67	2.20		After BP (Vacuum)
D4	1L WS ₂	10.63	6.24	1.70	300	After WS ₂
D5	1L WS ₂	4.56	3.24	1.40	300	After BP
D6	1L WS ₂	2.91	0.88	3.32	300	After WS ₂
D7	1L WS ₂	0.17	0.05	3.60	300	Not annealed
		0.25	0.05	4.82	205	

Supplementary Table 2: Role of barrier layer on tunnel diode performance

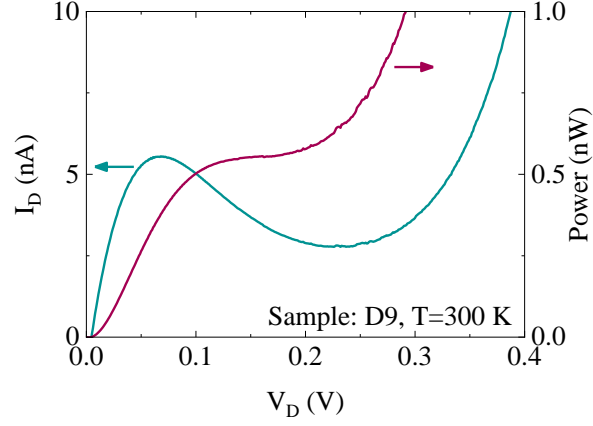
Device	Barrier	J_p (A/cm^2)	J_v (A/cm^2)	PVCR	Temperature (K)	Annealing
D8	None	21.90 (@V _D =0.5 V)		No NDR	300	Not annealed
D1	1L WS ₂	2.68	0.74	3.60	300	After WS ₂
D9	2L WS ₂	0.06	0.03	2.00	300	Not annealed
D10	1L MoS ₂	9.50	8.56	1.11	300	After MoS ₂



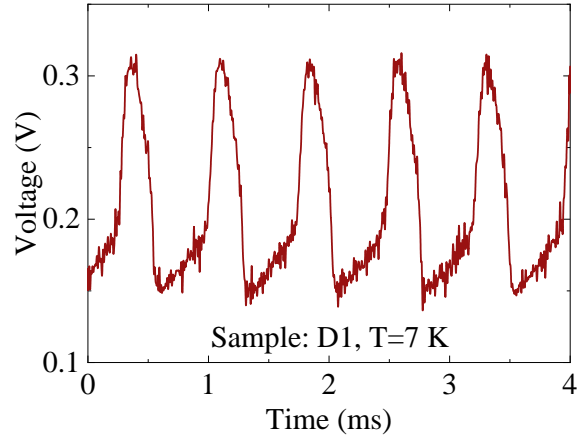
Supplementary Figure 3: **Different choice of barrier layers:** **a)** $I_D - V_D$ curves from samples with **a)** no barrier showing a large and linear tunnelling current, **b)** 1L-WS₂ barrier with a large PVCR, **c)** 2L-WS₂ barrier exhibiting moderate PVCR, but with a considerably lower I_P and **d)** 1L-MoS₂ barrier with a degraded PVCR.



Supplementary Figure 4: **Gate modulation of output characteristics:** **a)** $I_D - V_D$ curves from sample D4 employing a thin BP layer at 4.7 K as a function of gate bias ranging from 0 to -5 V. **b)** Left axis: Modulation of peak (empty teal circle markers) and valley (empty orange triangle markers) currents with gate bias. I_P increases with an increase in the negative V_G suggesting an increase in the p -type doping in BP. Right: Peak (solid teal circle markers) and valley (solid orange triangle markers) positions also exhibit a shift to higher voltages in accordance with the increasing drop across R_s as V_G approaches lesser negative values.



Supplementary Figure 5: **Absence of oscillation for 2L-WS₂ barrier:** Left axis: $I_D - V_D$ characteristics from sample D9 employing 2L-WS₂ as the tunnel barrier at 300 K showing no oscillations. Right: Power delivered corresponding to each applied V_D . Absence of multi-valued voltage at a given power further supports the disappearance of oscillations as we move to 2L-WS₂ barrier layer from 1L-WS₂.



Supplementary Figure 6: **Astable operation mode:** Temporal response from D1 at 7 K exhibiting oscillations when biased in the NDR regime.

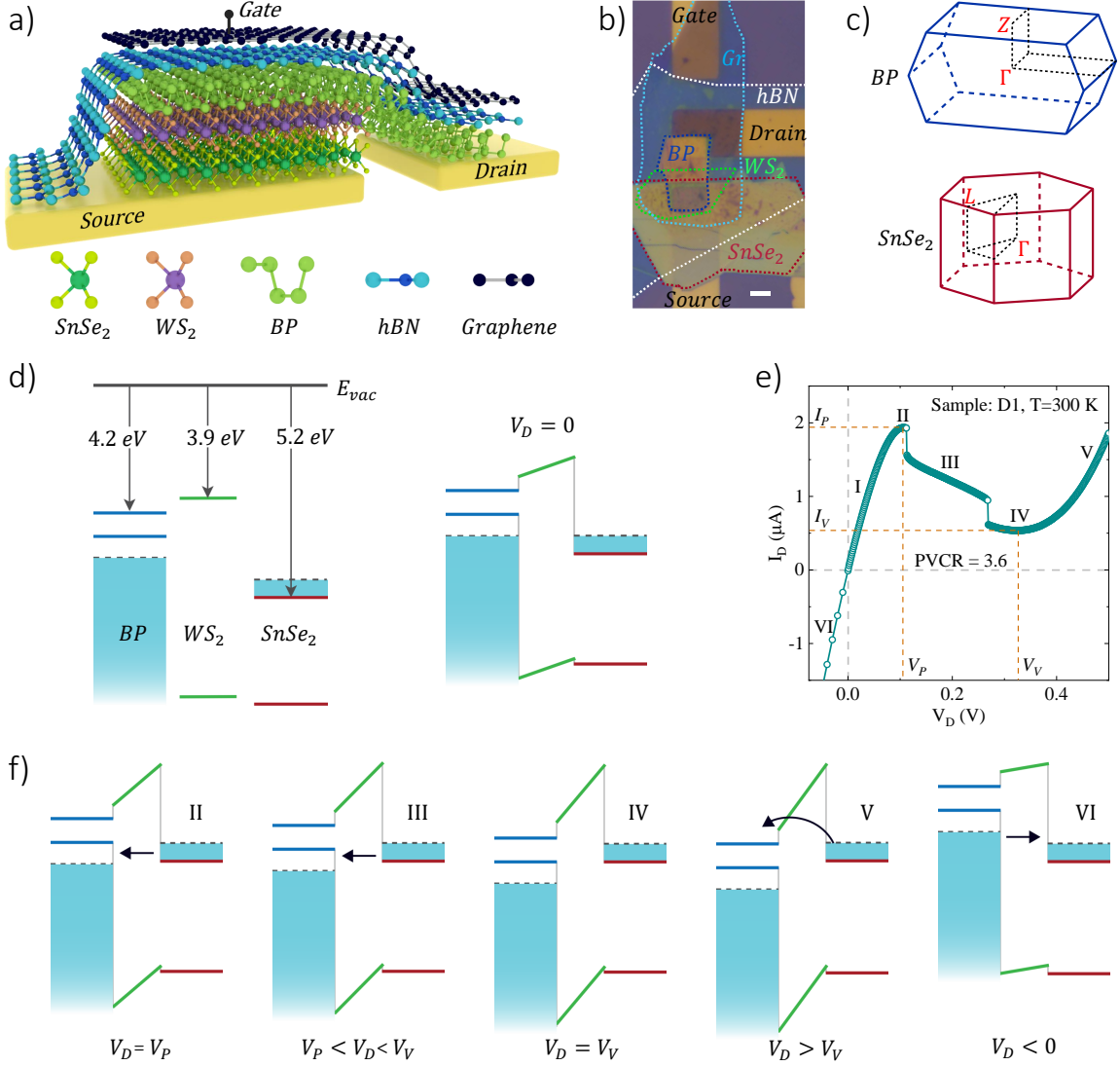


Figure 1: Tunnel diode operation: **a)** Schematic illustration of the SnSe₂/1L-WS₂/BP tunnel diode with an encapsulating hBN layer and a graphene gate. **b)** A representative optical image of the heterostructure outlining the various layers. Scale bar is 5 μm . **c)** Brillouin zones for bulk BP (top) and bulk SnSe₂(bottom). Z and L valleys correspond to valance band maxima of BP and conduction band minima of SnSe₂, respectively. **d)** Energy band alignment of the layers before (left) and after (right) contacting, suggesting broken gap alignment between BP and SnSe₂ with an ultra-thin 1L-WS₂ tunnel barrier. **e)** Measured output characteristics of the tunnel diode (D1) exhibiting a PVCR of 3.6 at 300 K. Various regions of operation under forward bias (Esaki mode) are marked as I through V, while the reverse bias (Zener mode) is shown as region VI. **f)** Energy band alignment for different regions of operation (see text for details). Black arrows indicate electron transport direction.

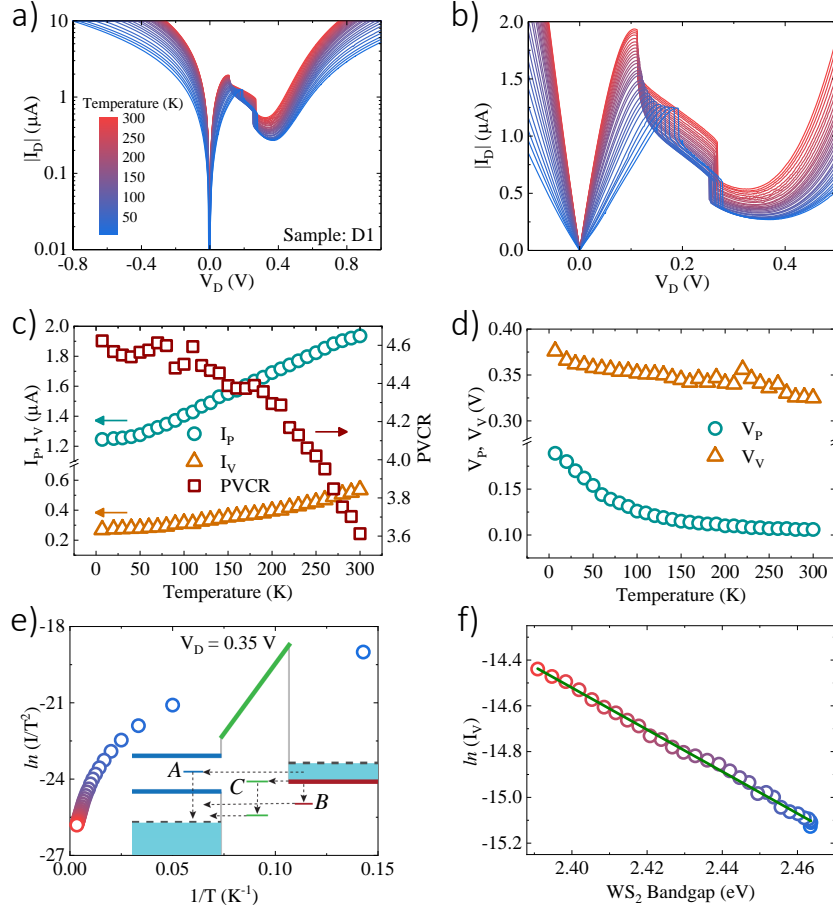


Figure 2: **Temperature dependence of tunnel diode characteristics:** **a)** $I_D - V_D$ curves from sample D1 at temperatures ranging from 7 to 300 K in log scale. **b)** Enlarged view of the NDR region in linear scale. **c)** Left axis: Extracted peak (circle markers) and valley (triangle markers) currents *versus* operating temperature. The strong temperature dependence for I_P suggests a phonon assisted tunnelling transport. Right axis: PVCR (square markers) of the device at each operating temperature. **d)** Variation of peak (circle markers) and valley (triangle markers) positions with temperature. **e)** Richardson plot for I_D near valley (@ $V_D = 0.35$ V) exhibiting a positive slope indicating an origin of valley current different from thermionic process. Color of the markers are mapped to the measurement temperature. Inset: various transport pathways through gap states for the generation of excess current. **f)** Variation of I_V with a temperature induced bandgap change of WS_2 (Circle markers with color mapped to temperature.). Good agreement with a the linear fit (green trace) suggest defect induced origin of excess current.

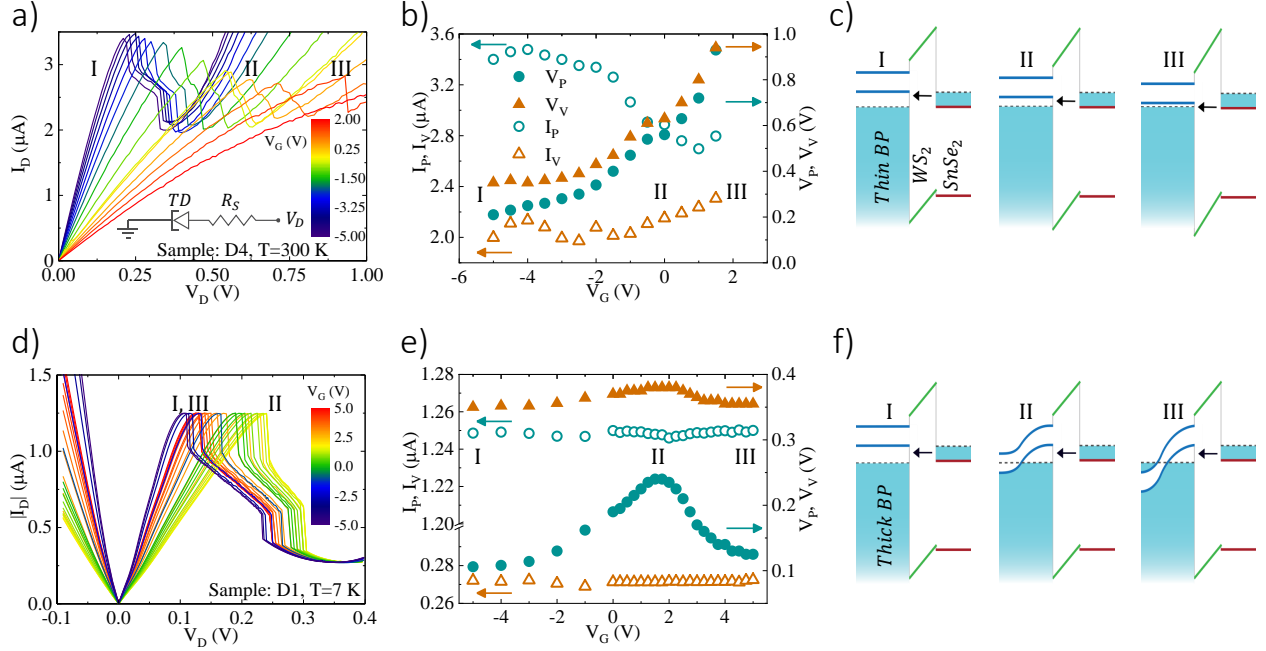


Figure 3: **Gate modulation of tunnel diode characteristics for thin and thick BP layers:** **a)** $I_D - V_D$ curves from sample D4 employing a thin BP layer at 300 K as a function of gate bias ranging from 2 to -5 V. Inset: An equivalent circuit of the heterostructure showing the series resistance of the lateral channel R_s and the tunnel junction. **b)** Left axis: Modulation of peak (empty teal circle markers) and valley (empty orange triangle markers) currents with gate bias. Increase in I_P is consistent with an increasing p -doping in BP at negative V_G . I_V being originating from excess current exhibit a weaker dependence on V_G . Right axis: Peak (solid teal circle markers) and valley (solid orange triangle markers) positions occurring at larger voltages with an increasing drop across R_s towards increasing V_G . **c)** Band alignment corresponding to I_P at negative V_G (I), near-zero V_G (II) and positive V_G (III). **d)** $I_D - V_D$ curves from sample D1 employing a thick BP layer at 7 K as a function of gate bias ranging from 5 to -5 V. **e)** Extracted peak and valley currents (left axis) and positions (right axis) from D1. Invariance of I_P with V_G suggests a fixed p -doping at the tunnelling interface. V_P and V_V gets modulated according to the variation of R_s with V_G . **f)** Band alignment at peak configuration corresponding to I) increased doping at the top interface of the BP channel at negative V_G , II) maximum channel resistance at slightly positive gate bias due to the depletion region formed near top of BP, III) e-h bilayer formation at the BP layer at further positive V_G and a subsequent reduction of R_s .

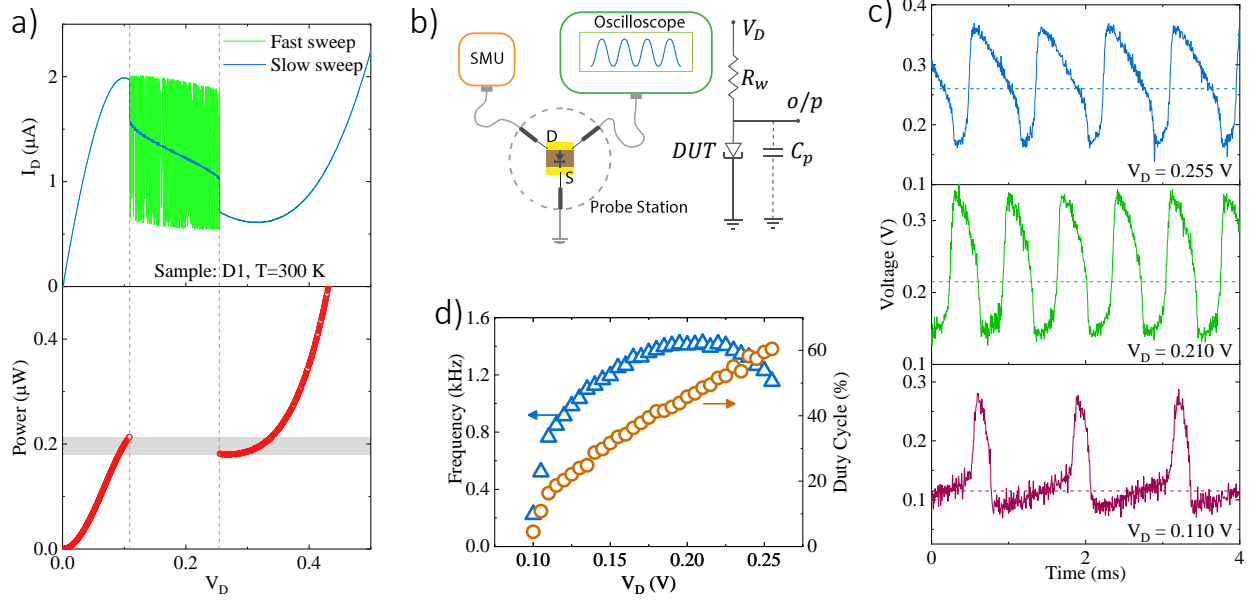


Figure 4: **Astable operation with intrinsic oscillations:** **a)** Top: $I_D - V_D$ curves from D1 at 300 K corresponding to slow (blue trace) and fast (green trace) V_D sweep exhibiting instability at the NDR region. Bottom: Power delivered to the system at each V_D . The grey shaded region indicates thermodynamic instability due to multi-valued voltage for a given power delivered. **b)** Schematic of measurement setup used for observing oscillations along with an equivalent circuit showing the parasitic effects limiting the high frequency operation. **c)** Temporal response of the system at three different biases showing variation of duty cycle as well as frequency of oscillation. **d)** Measured frequency (left axis, in blue triangle markers) and duty cycle (right axis, in orange circle markers) of oscillations as a function of biasing voltage V_D .

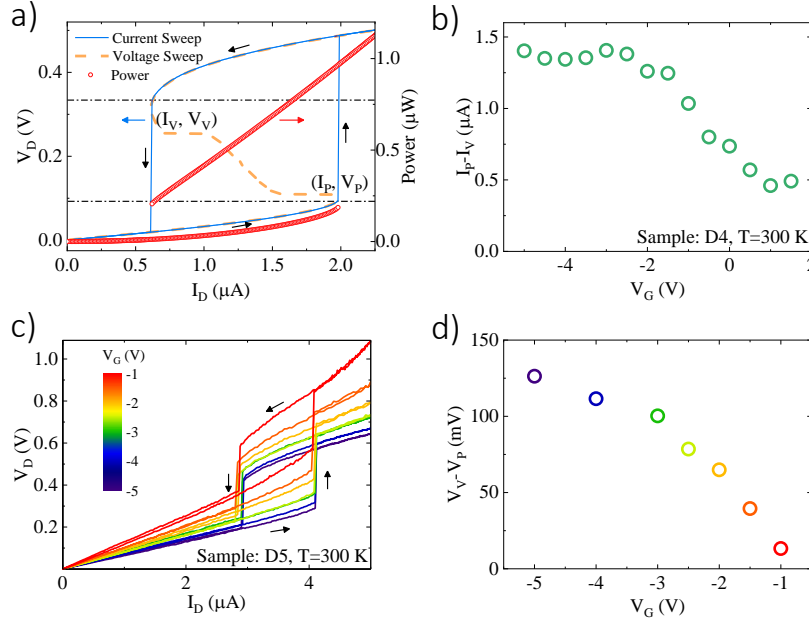


Figure 5: **Bistable operation with tunable memory cell:** **a)** Left axis: Results from a dual current sweep (blue trace) along with a voltage sweep (orange dashed trace) as a reference. Direction of the current sweep is indicated by black arrows. A bistable window between bias of I_P and I_V allows storage of information. Upper (lower) branch corresponds to a stored value of logic '1' (logic '0'). Right axis: Power delivered (red circle markers) to the system as a function of the current forced through the system. Multi-valued power for a given current bias indicates presence of metastable states separated by an energy barrier. **b)** Modulation of the write window from sample D4 at 300 K with V_G , suggesting a tunable noise performance. **c)** Output voltages from current sweep at V_G ranging from -1 to -5 V from sample D5 with thick BP at 300 K. **d)** Extracted read window tunability with V_G (color mapped to V_G) showing highly versatile memory operation.